Available online at www.sciencedirect.com
SCIENCE DIRECT®
Journal of Solid State Chemistry 179 (2006) 1303–1311
JOURNAL OF SOLID STATE CHEMISTRY
www.elsevier.com/locate/jssc

Electron doping effect on structural and magnetic phase transitions in $Sr_{2-x}Nd_xFeMoO_6$ double perovskites

A.K. Azad[a,*], S.-G. Eriksson[a], Abdullah Khan[b], A. Eriksson[a], M. Tseggai[c]

[a]*Department of Inorganic Chemistry, Göteborg University, SE-41296 Göteborg, Sweden*
[b]*Department of Chemistry, University of Balochistan, Quetta, Pakistan*
[c]*Department of Engineering Sciences, Uppsala University, SE-75121 Uppsala, Sweden*

Received 30 June 2005; received in revised form 18 January 2006; accepted 19 January 2006
Available online 21 February 2006

Abstract

Polycrystalline $Sr_{2-x}Nd_xFeMoO_6$ ($x = 0.0$, 0.1, 0.2, 0.4) materials have been synthesized by a citrate co-precipitation method and studied by neutron powder diffraction (NPD) and magnetization measurements. Rietveld analysis of the temperature-dependent NPD data shows that the compounds ($x = 0.0$, 0.1, 0.2) crystallize in the tetragonal symmetry in the range 10–400 K and converts to cubic symmetry above 450 K. The unit cell volume increases with increasing Nd^{3+} concentration, which is an electronic effect in order to change the valence state of the *B*-site cations. Antisite defects at the Fe–Mo sublattice increases with the Nd^{3+} doping. The Curie temperature was increased from 430 K for $x = 0$ to 443 K for $x = 0.4$. The magnetic moment of the Fe-site decreases while the Mo-site moment increases with electron doping. The antiferromagnetic arrangement causes the system to show a net ferrimagnetic moment.

Keywords: Double perovskite; Nuclear structure; Magnetic structure; Electron doping; Neutron diffraction; Magnetization measurement; CMR materials

1. Introduction

The recent discovery of the room temperature magnetoresistance in ordered double perovskite compounds [1–3] has generated intense interest in these materials because of their potential applications in magnetotransport devices as well as in their rich and challenging physical properties. Oxides of the type $A_2BB'O_6$ where A is an alkaline earth (A = Sr, Ca, Ba, …) and B, B' are heterovalent transition metals (B = Fe, Cr, …; B' = Mo, Re, …) are half metallic in nature with a high Curie temperature (above 400 K). This fact has stimulated a strong interest in these materials as a possible alternative to the mixed valence manganites. In Fe-based ordered double perovskite A_2FeMO_6 (A = Ca, Sr, Ba; M = Mo, Re) compounds, Fe^{3+} ($3d^5$, $S = 5/2$) and Mo^{5+} ($4d^1$, $S = 1/2$) [or Re^{5+} ($5d^2$, $S = 1$)] couple antiferromagnetically, where the conduction band is composed of the 4*d* (5*d*) down-spin electrons of Mo^{5+} (or Re^{5+}). Therefore these materials can be regarded as half-metallic ferrimagnets (FiM) showing high magnetic Curie temperature (T_C) [4–6]. However, these materials can also be regarded as ferromagnetic (FM) because Mo or Re are intrinsically nonmagnetic in the sense that their magnetic polarization cannot be sustained spontaneously by the exchange potential on these atoms. The T_C in Sr_2FeMoO_6 was found to decrease irrespective of the ionic size of substituting divalent ions (Ca^{2+} or Ba^{2+}) as the amounts of substitution increased [7,8]. The observed variation in T_C and the crystallographic structure has been investigated as a function of the average ionic radius ($\langle r_A \rangle$) [9,10]. A high spin-polarization of conduction carriers expected for Sr_2FeMoO_6 is attractive in the light of the potential application within magnetoresistive devices. A relatively high magnetic transition temperature (410–450 K) indicates that a spin-polarization of the conduction electrons remains relatively high (70%) even at room temperature. Recently, it has been observed that carrier doping in A_2FeMoO_6 double perovskites can increase the FM transition temperature [11–14]. A 70 K increase in T_C by La doping was reported in polycrystalline

*Corresponding author. School of Chemistry, University of St. Andrews, Fife KY16 9ST, Scotland, UK. Fax: +44 1334 46 3808.
E-mail address: aka7@st-andrews.ac.uk (A.K. Azad).

0022-4596/$ - see front matter © 2006 Elsevier Inc. All rights reserved.
doi:10.1016/j.jssc.2006.01.043

$Sr_{2-x}La_xFeMoO_6$ ($0<x<1$) [11]. It has been observed that this substitution adds electrons to the B/B' sublattices and an increase of the electron density at the Fermi level. Calculation of the mean field model suggests that the magnitude of the FM coupling is directly related to the density of electrons at the Fermi level [15]. Therefore, the injection of electrons into the conduction band by appropriate doping ions emerges FM interactions and increases the Curie temperature (T_C). It is evident that electron doping by La increases the antisite (AS) defect concentration, which lowers the saturation magnetization [11]. In fact even in pure samples a reduced magnetic moment is present that strongly depends on the synthesis process, purity and AS displacement of the B-site atoms [16,17]. In this respect, it is interesting to observe the possible modification in structural and magnetic properties caused by Nd^{3+} doping. Very recent studies on this system based on Mössbauer [18], X-ray and magnetization measurements [19] has described the possible Fe–Mo valence state and increased T_C.

In this paper, we have investigated the effects of partial substitution of Sr^{2+} by Nd^{3+} on the structural, magnetic and electronic properties in the conducting double perovskite $Sr_{2-x}Nd_xFeMoO_6$ (SNFMO) by neutron powder diffraction (NPD) and magnetization measurements. We observed that charge doping, i.e. modification of the density of charge carriers in the conduction band provides an efficient way to increase the Curie temperature. By means of NPD measurements, we have determined the respective magnetic moments of the magnetic cations.

2. Experimental

Polycrystalline SNFMO samples were prepared by a citrate co-precipitation method. Stoichiometric amounts of high purity powder of $Sr(NO_3)_2$ (BDH Chemicals Ltd.),

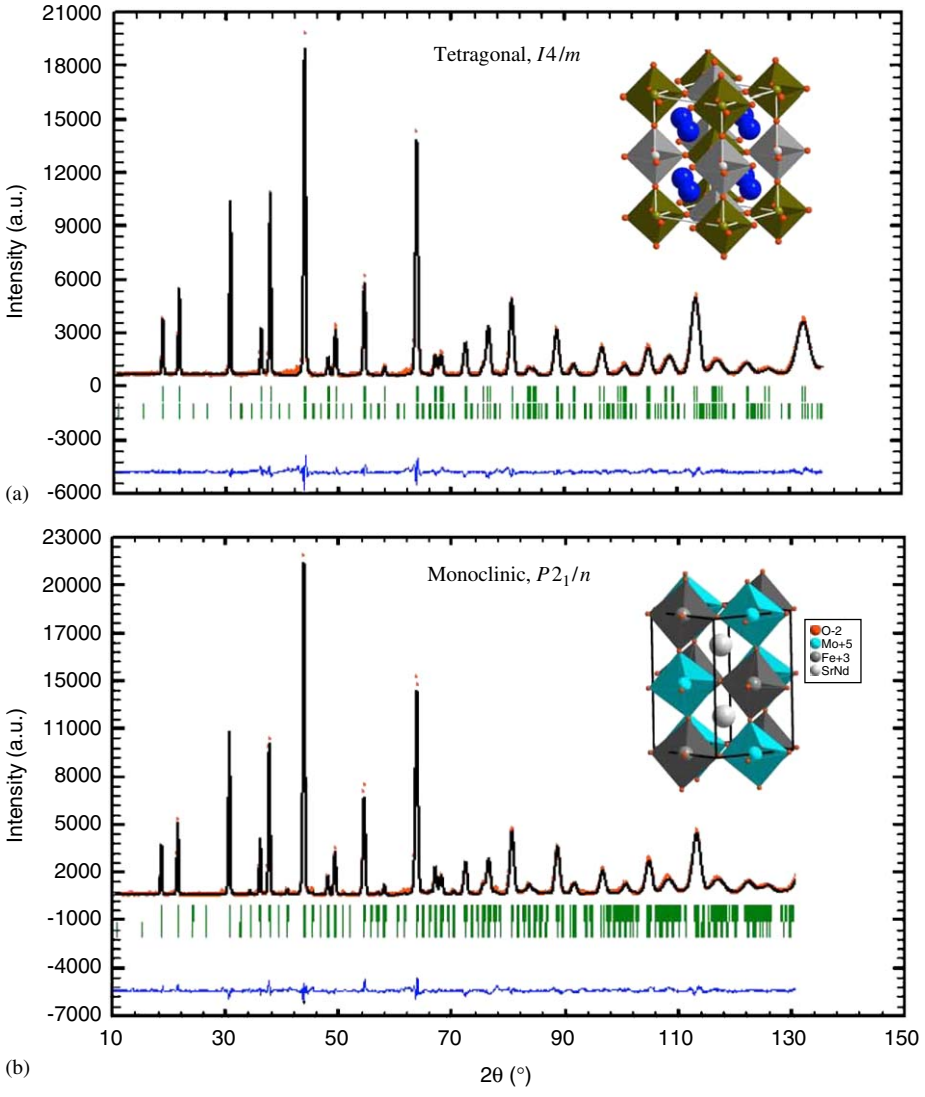

Fig. 1. Observed (circles) and calculated (continuous line) NPD intensity profiles for $Sr_{2-x}Nd_xFeMoO_6$ ($x=0.1$) (a) and $x=0.4$ (b) at 10 K. The short vertical lines indicate the angular position of the allowed Bragg reflections. The 2nd vertical lines are the Bragg reflections from magnetic structure. At the bottom in each figure the difference plot, I_{obs}–I_{calc}, is shown. 3D schematic polyhedral views are shown in the insertions.

$FeC_2O_4 \cdot 2H_2O$ (Sigma-Aldrich Chem.) and $(NH_4)_6Mo_7O_{24} \cdot 4H_2O$ (Sigma-Aldrich Chem.) were mixed in a glass bowl. About 250 ml distilled water was added to the mixture and then concentrated HNO_3 was added slowly until the mixture was completely dissolved. Stoichiometric amount of citric acid ($C_6H_8O_7 \cdot H_2O$) was added in 1:1:1:1 ratio and heated at 75 °C for 1 h. Then the heat was gradually increased to 250 °C for several hours to form the gel-like precipitate which finally resulted into polycrystalline powder. The materials were sintered in air at 300 °C for 2 h, 500 °C for 8 h and 800 °C for 4 h. Then the powders were pressed into pellets and heated at 1050 °C in Ar + 5% H_2 for 12 h. All heat treatments were performed using alumina crucibles and with a slow increase (2°/min) and decrease (4°/min) in temperature.

The identification of phases and determination of room temperature lattice constants were accomplished using a Guinier–Hägg focusing camera (Cu$K\alpha_1$, $\lambda = 1.540598$ Å) with Si as internal standard. Indexing and refinement of the lattice parameters were made using the programs TREOR90 [20] and Checkcell [21], respectively. NPD data were collected at the NPD neutron diffractometer of the Studsvik Neutron Research Laboratory, Sweden in the temperature range 10–500 K. The double monochromator system consisting of two parallel copper crystals in (220) orientation was aligned to give a wavelength of 1.470(1) Å. The neutron flux at the sample position was approximately 10^6 neutrons cm^{-2} s^{-1}. The step scan covered the 2θ-range 4–139.92° with a step size of 0.08°. NPD data sets were refined by the Rietveld method using the FullProf software [22]. A magnetic phase was included in the refinement as a second phase for which the Fe, Mo and Nd cations were defined.

DC magnetization measurements were performed using a Quantum Design SQUID magnetometer in the temperature range $300\,K \leqslant T \leqslant 500\,K$ and the applied magnetic fields from 0 to 50 kOe.

3. Results and discussion

We have observed that NPD data on $Sr_{2-x}Nd_xFeMoO_6$ ($x = 0.0, 0.1, 0.2$) can be well refined in the tetragonal $I4/m$ space group (No. 87, $Z = 2$). Recent group theoretical analysis shows that $I4/m$ is the most probable space group for $x = 0$ materials [23] although it can also be refined in $I4/mmm$ [16] and $P4_2/m$ [8]. For the composition $x = 0.4$ i.e. 20% of Nd^{3+} doping at the A-site, some extra reflections appear in the diffraction pattern which is forbidden in the I-centered tetragonal symmetry. It was observed that the monoclinic $P2_1/n$ space group can define those reflections like (311)/(131). In Glazer's notation, these symmetries correspond to a change from the $a^0a^0c^-$ ($I4/m$) to the $a^+b^-b^-$ ($P2_1/n$) tilt system [24]. This change in symmetry can be attributed to the small size of Nd^{3+} (compared to that of the Sr^{2+} ion) which reduces the Goldschimdt tolerance factor (t) of the perovskite structure, thus inducing the rotation of FeO_6 and MoO_6 octahedra. Fig. 1a and b shows the Rietveld refinement profile of the neutron diffraction data for $Sr_{1.9}Nd_{0.1}FeMoO_6$ and $Sr_{1.6}Nd_{0.4}FeMoO_6$ at 10 K in the $I4/m$ and $P2_1/n$ space groups, respectively. The superstructure reflections (e.g. (011) and (013) in the tetragonal symmetry) were observed, due to the ordering of Fe and Mo atoms on the octahedral B-sites of the perovskite structure. The unit cell parameters are related to that of ideal cubic perovskite as $a \approx \sqrt{2}a_p$, $b \approx \sqrt{2}a_p$, $c \approx 2a_p$($a_p \approx 3.89$ Å) in both space groups. Relevant structural details obtained from NPD data refinement at 10 K are reported in Table 1. Above 450 K the structure of the compounds for $x = 0.0$, 0.1 and 0.2 converts to cubic symmetry (space group $Fm3m$, No. 225) and for $x = 0.4$ it change to the tetragonal symmetry ($I4/m$). Fig. 2 shows the variation of lattice parameters as a function of temperature for $x = 0.1$ and Fig. 3 shows the

Table 1
Main crystallographic and magnetic information for $Sr_{2-x}Nd_xFeMoO_6$ from Rietveld refinement of the NPD data at 10 K

Space group	$x = 0$	$x = 0.1$	$x = 0.2$	$x = 0.4$
	$I4/m$	$I4/m$	$I4/m$	$P2_1/n$
a (Å)	5.5529(4)	5.5557(5)	5.5625(5)	5.5609(5)
b (Å)	—	—	—	5.5578(5)
c (Å)	7.8993(5)	7.8877(6)	7.8807(6)	7.8884(6)
β (deg.)	—	—	—	89.72(7)
V (Å^3)	243.57(5)	243.46(5)	243.84(6)	243.81(6)
AS (%)	3.2	9.2	14.4	37.2
Sr/Nd	4d ($\frac{1}{2}0\frac{1}{4}$)	4d ($\frac{1}{2}0\frac{1}{4}$)	4d ($\frac{1}{2}0\frac{1}{4}$)	4e (xyz)
x	0.5	0.5	0.5	−0.0005(3)
y	0.0	0.0	0.0	0.0144(5)
z	0.25	0.25	0.25	0.2554(5)
B (Å^2)	0.24(7)	0.26(8)	0.27(5)	0.23(7)
Fe	2a (000)	2a (000)	2a (000)	2c ($0\frac{1}{2}0$)
B (Å^2)	0.19(5)	0.25(3)	0.26(4)	0.29(7)
Mo	2b ($00\frac{1}{2}$)	2b ($00\frac{1}{2}$)	2b ($00\frac{1}{2}$)	2d ($\frac{1}{2}00$)
B (Å^2)	0.17(3)	0.24(4)	0.23(5)	0.28(5)
O1	4e (00z)	4e (00z)	4e (00z)	4e (xyz)
x	0.0	0.0	0.0	0.2605(5)
y	0.0	0.0	0.0	0.2621(4)
z	0.2528(5)	0.2529(4)	0.2532(5)	0.0131(6)
B (Å^2)	0.27(4)	0.29(5)	0.36(5)	0.46(6)
O2	8h (xy0)	8h (xy0)	8h (xy0)	4e (xyz)
x	0.2759(5)	0.2706(5)	0.2741(6)	0.2751(5)
y	0.2267(6)	0.2245(5)	0.2235(5)	0.2685(5)
z	0.0	0.0	0.0	0.4779(6)
B (Å^2)	0.28(6)	0.30(5)	0.36(4)	0.48(6)
O3	—	—	—	4e (xyz)
x	—	—	—	0.5522(4)
y	—	—	—	−0.0005(3)
z	—	—	—	0.2456(5)
B (Å^2)	—	—	—	0.11(6)
μ_{Fe}	3.78(7)	3.33(8)	3.07(6)	1.45(7)
μ_{Mo}	−0.49(7)	−0.70(8)	−0.78(6)	0.94(3)
μ_{Nd}	—	−0.06(4)	−0.08(5)	0.12(6)
R_p (%)	4.40	4.71	7.11	5.22
R_{wp} (%)	5.86	6.23	10.6	7.55
R_{Bragg} (%)	3.37	2.92	5.22	4.07
R_{mag} (%)	5.75	6.36	5.69	2.84
χ^2	4.28	4.85	6.26	6.30

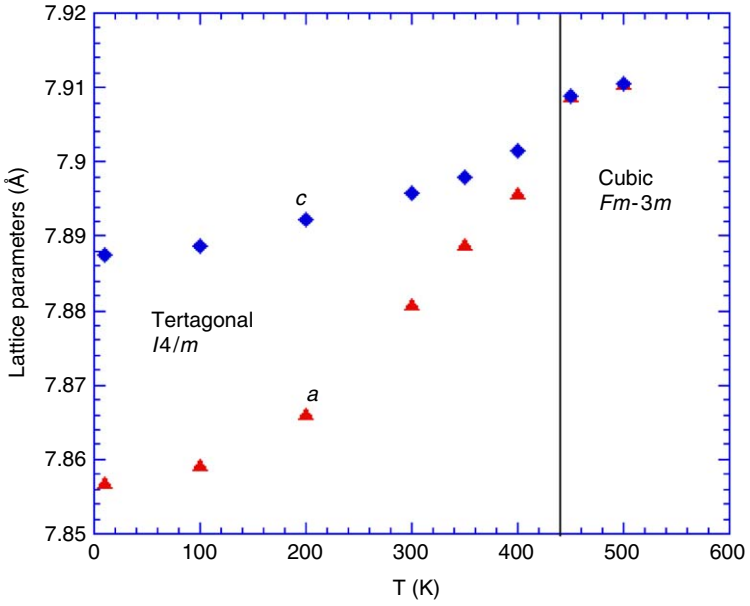

Fig. 2. Variation of lattice parameters as a function of temperature. In the tetragonal phase, the values of lattice parameter a are multiplied by $\sqrt{2}$ for comparison.

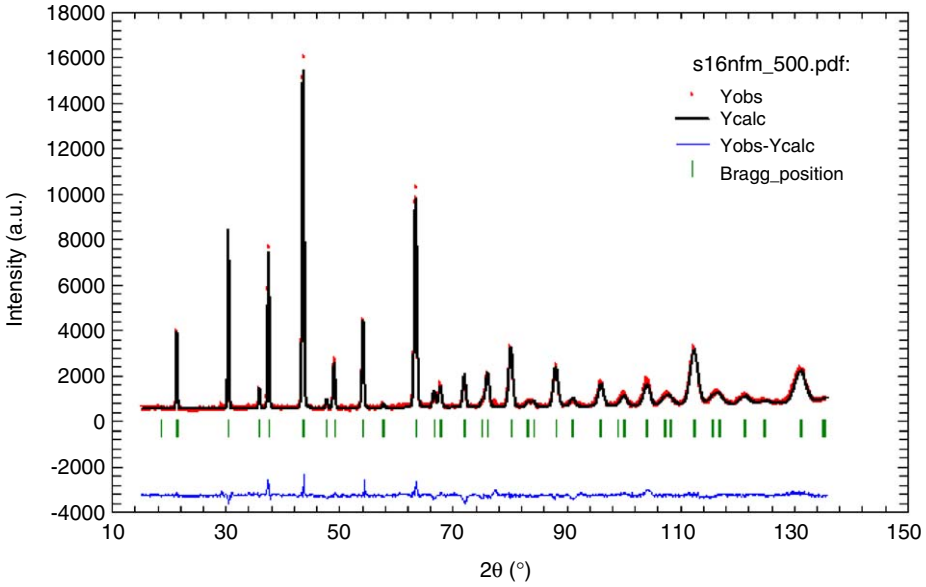

Fig. 3. Rietveld refinement profile for $x = 0.4$ in the space group $I4/m$ at 500 K.

Rietveld refinement profile for $x = 0.4$ in tetragonal symmetry.

The lattice parameters increase with electron doping. The expansion of the unit cell parameters upon doping with a smaller volume cation is opposite to what is expected from Vegard's law. The change of cell volume with electron doping shows a sharp deviation from Vegard's law that can be interpreted as a progressive change from itinerant to localized electronic behavior of the majority spin electrons. Since the tolerance factor decreases, the cell expansion is not motivated by the steric effects associated with the ionic sizes but it reflects electronic effects. Substitution of a divalent cation by trivalent cation results in electron doping into the antibonding orbitals of t_{2g} and e_g parentage of Fe and Mo ions. A well-defined antiferromagnetic (AFM) interaction results between the itinerant electrons and the Fe localized cores, driven by the hopping of the electrons between Fe- and Mo-sites [1,25]. As described in the Virial theorem, which for central-force fields states that

$$2\langle T\rangle + \langle V\rangle = 0.$$

An increase in mean kinetic energy $\langle T\rangle$ as more minority-spin electrons become localized requires an

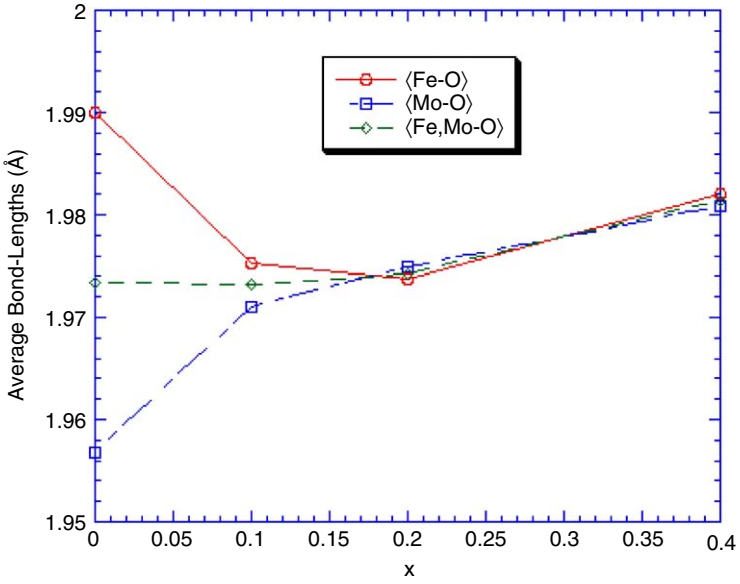

Fig. 4. The change of average bond distances with Nd doping.

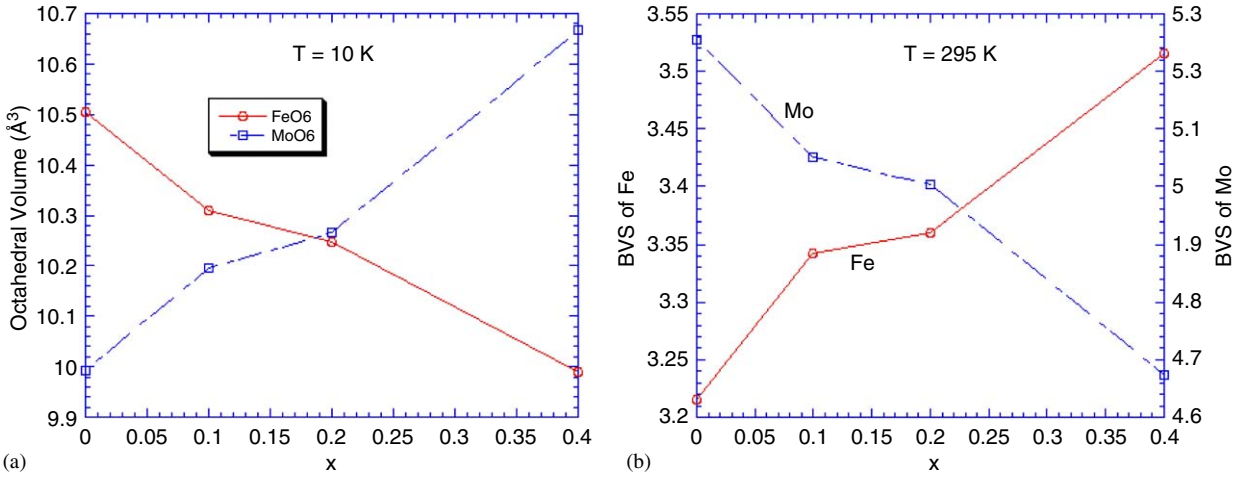

Fig. 5. (a) Variation of *B*-site octahedral volume with composition at 10 K and (b) variation of bond valence sum of Fe and Mo valence state with Nd doping.

increase in the magnitude $|\langle V\rangle|$ of the mean potential energy. For antibonding electrons, an increase in $|\langle V\rangle|$ is accomplished by an increase in the mean equilibrium Fe–O–Mo bond length, which is relevant to an increase in the cell volume with electron doping [26]. Nd doping increases the density of electrons at the Fermi level as well as promotes a structural distortion for the concentration above 20%. As a result of it, the observed enhancement of electron density at the Fermi level is attributed to a band-filling effect. The mean bond distance $\langle d_{\mathrm{Fe-O}}\rangle$ decreases and, $\langle d_{\mathrm{Mo-O}}\rangle$ as well as $\langle d_{\mathrm{(Fe,Mo)-O}}\rangle$ increases with Nd doping (Fig. 4). Thus the increase in T_C is due to the electron filling of the conduction band [27]. The small anomaly in $\langle d_{\mathrm{Fe-O}}\rangle$ bond length for $x = 0.4$ is due to the structural-phase change from tetragonal to monoclinic symmetry.

According to the Shannon [28], the effective ionic radius (r_i) of Fe^{2+} ($r_i = 0.78$ Å) is greater than that of the ionic radius of Fe^{3+} ($r_i = 0.645$ Å). The increase in lattice parameters is related to the change of Fe^{3+} or Mo^{5+} to a lower valence state. If Fe^{3+} changes to Fe^{2+}, Mo^{5+} ($r_i = 0.61$ Å) needs to be changed to Mo^{6+} ($r_i = 0.59$ Å) in order to accomplish charge balance. However, calculation of FeO_6 and MoO_6 octahedral volume for different compositions (Fig. 5a) shows that the volume of FeO_6 decreases and the volume of MoO_6 increases with increasing Nd doping. This indicates the existence of lower valent Mo^{4+} ($r_i = 0.65$ Å) which can increase the octahedral volume. Calculations of the Bond Valence Sum (BVS) at RT using Brown's bond valence model [29], from the average bond distances ($d \leqslant 3.5$ Å) between Fe–O and Mo–O (using the initial valence state of Fe and Mo as Fe^{3+}

and Mo^{5+}) show that the Fe valence increases from +3.22 to +3.52 and the Mo valence decreases from +5.26 to +4.68 with 20% Nd doping at the *A*-site (Fig. 5b). In the case of AS defect, the valence state follows the average site valences i.e. ($Fe^{3+}_{1-x}Mo^{5+}_{x}$) and ($Mo^{5+}_{1-x}Fe^{3+}_{x}$) at the *B*- and *B*′-sites, respectively. Rietveld refinement of NPD data show that the occupancy of Mo at the Fe-site and Fe at the Mo-site increases with the Nd concentration. As more Mo^{5+} enters the Fe^{3+}-site the site valence increases and when more Fe^{3+} is mixed at the Mo^{5+}-site, the site valence decreases. The effect of the electron doping is mainly received by AS Mo atoms, which being surrounded by six $Mo^{5+/6+}$ atoms, prefer the lower $Mo^{5+/4+}$ valence state. This result is in accordance to the findings from Mössbauer spectroscopy [18]. As shown in Fig. 4 the average Fe/Mo–O bond distances increase with the electron doping i.e. the extra electrons fill the conduction band and thus increases the mean kinetic energy which then increases the cell volume. The electron doping which leads to an increased ionic radii of the atomic species at the (*B*, *B*′) sites and the reduction of the mean size of the (*A*, *A*′) cations leads to a decrease in the tolerance factor thus justifying the reduction of symmetry upon doping. Due to this reason the high-temperature cubic phase is stabilized at somewhat higher temperature than 500 K when $x = 0.4$.

For all compositions, the low temperature (10 K) NPD data reveal a strong magnetic contribution on the low-angle reflections. In the magnetic phase, space group *P*1 was used with the magnetic moment defined for the Fe, Mo and Nd positions (although the magnetic contribution of Mo and Nd is very small). Mo and Nd magnetic moment directions are parallel with each other but antiparallel with the direction of the Fe moment giving a global ferrimagnetic arrangement (Fig. 6). This model gives an acceptable goodness-of-fit and *R*-factors. Magnetic *R*-factors are <6% for all compounds. The final refinement parameters at 10 K for different compositions are listed in Table 1. The ordered magnetic moment on the Fe-site decrease from 3.86(1) to 3.07(3) μ_B, the ordered magnetic moment on the Mo-site increases from 0.54(4) to 0.94(3) μ_B with increasing Nd concentration at the *A*-site. The same magnetic model was used to refine all the remaining data sets from 10–400 K. Fig. 7(a) shows the thermal evolution of the ordered magnetic moment at the Fe positions for different compositions. The magnetic moment decreases with the increasing temperature is due to the disorder in the long-range ordering, and above Curie temperature no magnetic order is observed. The superexchange interaction was established between Fe atoms via Mo atoms as Fe–O–Mo–O–Fe. When the disorder between Fe and Mo atoms increases, the direct Fe–O–Fe superexchange interaction also increases. The enhancement of the magnetic moment is linearly related with the enhancement of Curie temperature [30]. The change in magnetic moment at the *B*-site is related

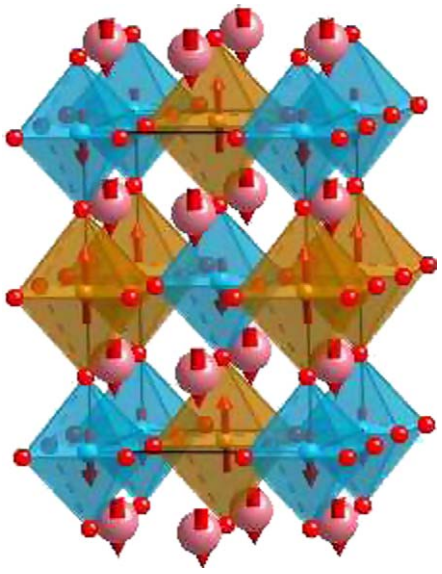

Fig. 6. 3D magnetic structure of $Sr_{1.6}Nd_{0.4}FeMoO_6$ indicating the direction of magnetic moment at Fe, Mo and Nd positions.

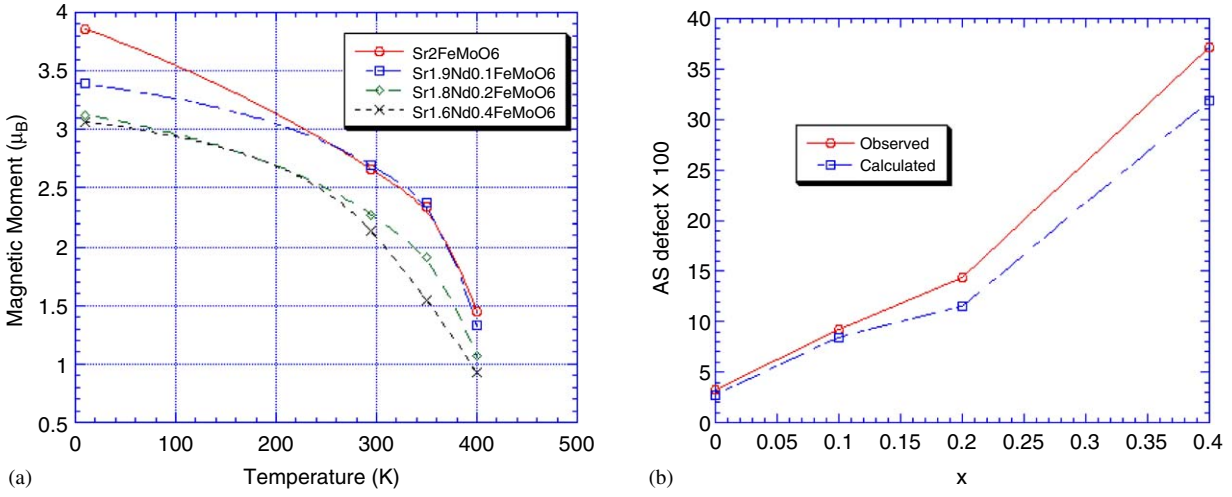

Fig. 7. (a) Variation of magnetic moment of Fe with temperature for different compositions and (b) variation of observed and calculated antisite defect concentration with electron doping.

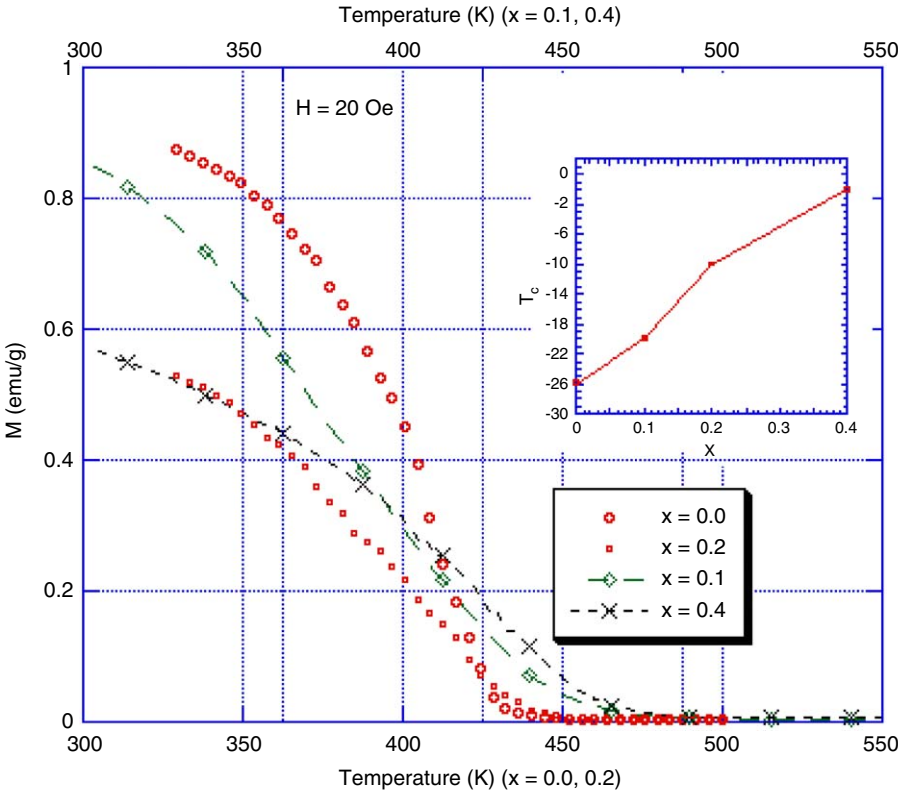

Fig. 8. M_{FC}/H versus temperature graphs for different compositions measured with the applied fields $\mu_0 H = 20$ Oe. Curie temperature (T_C) versus composition (x) is plotted in the inset.

to the increasing AS defects; as the number of AS defects increases the magnetic moment decreases. For an ideal ferrimagnetic ordering at the B-site of the double perovskite can be written as, $M_B = M_{B'} - M_{B''}$. Assuming spin only magnetic moment of Fe^{3+} as $5\,\mu_B$ and for Mo^{5+} as $1\,\mu_B$, $M_B = 4\,\mu_B$. Considering the FM interaction between Fe cations, we have observed that the AS defect concentration obtained from Rietveld refinement of NPD data is well comparable with the AS defect concentration obtained from the calculation using the formula, $p = [(M_B - M_{Fe})/8]$ μ_B/formula unit (Fig. 7b), where p is the AS-site defect concentration.

All samples show typical FM ordering. The magnetization versus temperature data, at an applied field of 20 Oe (Fig. 8), shows low-temperature saturation characteristic of a spontaneous FM ordering. The magnetization versus magnetic field data shown in Fig. 9 at 5 K are characteristic of a ferromagnet with a saturation magnetization of about $2.8\,\mu_B$/formula unit for $x = 0$ sample. The first derivatives of the $M(T)$ curves gives the value of the Curie temperature T_C. The $M(T)$ characteristics were measured in two different intervals, so, two x-axes are used in the Fig. 8. It is evident from the figure that T_C increases upon Nd doping. It is worth mentioning that for $x = 0.0$, T_C is 430 K, which is higher than earlier reported values [1,17]. The rise in T_C in Sr_2FeMoO_6 could be related to the optimized synthesis process controlling the crystallite size, homogeneity and the AS defect concentration of the materials. Otherwise sol–gel prepared small-scale grain samples can show lower magnetic transition temperatures and larger magnetoresistance due to the strong disorder effect from more grain boundaries [31]. In our sample for $x = 0$, we have observed very small amount of B-site disorder which could be one of the reasons why we obtained a higher magnetic transition temperature. As shown in Fig. 9 the magnetization of the samples decreases as the Nd concentration increases. This is related to the increase in AS defect level when Nd is introduced into the structure. It is observed from the $M(H)$ measurements that the magnetization does not saturate at high field (up to 50 kOe). Our results from NPD refinement show that the magnetic moment of Nd^{3+} varies from 0.2 to $0.9\,\mu_B$ for 5–20% Nd doping at 10 K, which is similar to the value observed in $(Nd_{0.7}A_{0.3})MnO_3$ (A = Sr, Ba, Pb) at 4.2 K [32]. Saturation magnetization (M_S) as well as the Fe-site moment decrease rapidly upon Nd doping. This decrease of saturation moment is the effect of increase of AS defect concentration. If we consider this saturation magnetization as a result of ideal ferrimagnetic interaction between Fe- and Mo-site moments only, in a simple picture for Fe^{3+} and Mo^{5+} ions, $M_S = \mu_{Fe} - \mu_{Mo} = 5 - 1 = 4\,\mu_B$/formula unit. Monte Carlo simulation studies showed that the rate of the decrease in M_S is $0.08\,\mu_B/p$ [33]. According to the Goodenough–Kanamori rules, the d^5:d^1 and d^5:d^5 super-exchange interactions are all AFM, and thus atomic AS defect do not appear to introduce any magnetic frustration.

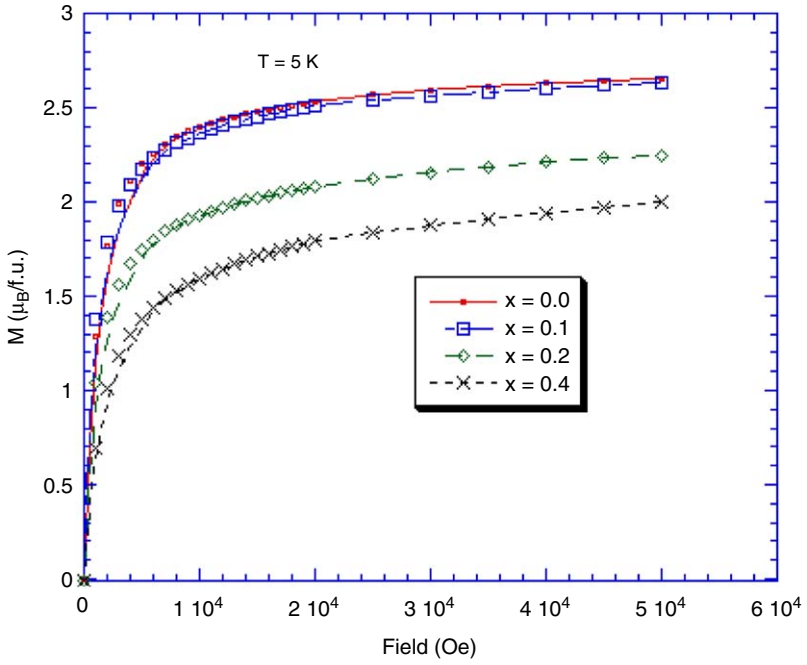

Fig. 9. Magnetization versus applied field measured at 5 K.

Our findings of AS AFM coupling between Fe- and Mo-sites supports these predictions and the reduction of magnetization is the combined effect of AS defect concentration and electron injection into the spin down band.

4. Conclusions

We have reported upon citrate co-precipitation synthesis of the $Sr_{2-x}Nd_xFeMoO_6$ ($x = 0.0$, 0.1, 0.2, 0.4) materials, nuclear and magnetic structure from NPD experiments and magnetic susceptibility from magnetization measurements. Mainly, the following observations have been found in the present study.

(1) Structural symmetry changes from tetragonal ($x = 0.0$, 0.1, 0.2) to monoclinic ($x = 0.4$) upon Nd^{3+} doping. A high-temperature NPD study showed that samples showing tetragonal symmetry (space group $I4/m$) changed to cubic symmetry (space group $Fm3m$) while samples with monoclinic symmetry (space group $P2_1/n$) changed to tetragonal symmetry (space group $I4/m$) above 450 K.
(2) Electron doping has very little effect on the Fe valence to change from Fe^{3+} to Fe^{2+} and Mo valence to change from Mo^{5+} to Mo^{6+}, but stronger effect on the Mo valence to change from Mo^{5+} to Mo^{4+}.
(3) The ferrimagnetic to paramagnetic transition temperature increased from 430 K ($x = 0$) to 443 K ($x = 0.4$) whereas saturation magnetization decreased from 2.8 μ_B/formula unit to 2.3 μ_B/formula unit with an increase in Nd concentration at the A-site.
(4) The AS defect concentration increased with the electron doping i.e. the electron donor character of the A-site cation showed a strong influence on the AS defect concentration at the B-site.
(5) The average magnetic moment of the Fe-sites decreased and at the Mo- and Nd-sites increased with electron doping. The Mo- and Nd-site moments are arranged ferromagnetically with each other but antiferromagnetically with respect to the Fe-site moment.

Acknowledgments

The authors are grateful to the Swedish foundation of Strategic Research (SSF) for financial support via OXIDE project. One of the authors, A.K. Azad, is grateful for the financial support from "Research, development and training project of Bangladesh Atomic Energy Commission". A. Khan acknowledges the financial support from Higher Education Commission (HEC), Pakistan.

References

[1] K.-I. Kobayashi, T. Kimura, H. Sawada, K. Terakura, Y. Tokura, Nature 395 (1998) 677.
[2] H. Kato, T. Okuda, Y. Okimoto, Y. Tomioka, Y. Takenoya, A. Ohkubo, M. Kawasaki, Y. Tokura, Appl. Phys. Lett. 81 (2002) 328.
[3] W. Westerburg, O. Lang, C. Ritter, C. Felser, W. Tremel, G. Jakob, Solid State Commun. 122 (2002) 201.
[4] K.-I. Kobayashi, T. Kimura, Y. Tomioka, H. Sawada, K. Terakura, Y. Tokura, Phys. Rev. B 59 (1999) 11159.
[5] T.H. Kim, M. Uehara, S.-W. Cheong, S. Lee, Appl. Phys. Lett. 74 (1999) 1737.
[6] A. Maignan, B. Raveau, C. Martin, M. Hervieu, J. Solid State Chem. 144 (1999) 224.

[7] J.A. Alonso, M.T. Casais, M.J. Martínez-Lope, J.L. Martínez, P. Velasco, A. Muñoz, M.T. Fernández-Díaz, Chem. Mater. 12 (2000) 161.
[8] C. Ritter, M.R. Ibarra, L. Morellon, J. Blasco, J. García, J.M. De Teresa, J. Phys.: Condens. Matter 12 (2000) 8295.
[9] R.P. Borges, R.M. Thomas, C. Cullinan, J.M.D. Coey, R. Suryanarayanan, L. Ben-Dor, L. Pinsard-Gaudart, A. Revcolevschi, J. Phys.: Condens. Matter 11 (1999) L445.
[10] J. Navarro, C. Frontera, Ll. Balcells, B. Martínez, J. Fontcuberta, Phys. Rev. B 64 (2001) 092411.
[11] H.M. Yang, W.Y. Lee, H. Han, B.W. Lee, C.S. Kim, J. Appl. Phys. 93 (2003) 6987.
[12] J. Navarro, J. Nogués, J.S. Muñoz, J. Fontcuberta, Phys. Rev. B 67 (2003) 174416.
[13] W.R. Branford, S.K. Clowes, Y.V. Bugoslavsky, Y. Miyoshi, L.F. Cohen, J. Appl. Phys. 94 (2003) 4714.
[14] D. Serrate, J.M. De Teresa, J. Blasco, M.R. Ibarra, L. Morellón, C. Ritter, Appl. Phys. Lett. 80 (2002) 4573.
[15] M. Tovar, M.T. Causa, A. Butera, J. Navarro, B. Martínez, J. Fontcuberta, M.C.G. Passeggi, Phys. Rev. B 66 (2002) 024409.
[16] O. Chmaissem, R. Kruk, B. Dabrowski, D.E. Brown, X. Xiong, S. Kolesnik, J.D. Jorgensen, C.W. Kimball, Phys. Rev. B 62 (2000) 14197.
[17] D. Sánchez, J.A. Alonso, M. García-Hernández, M.J. Martínez-Lope, J.L. Martínez, A. Mellergård, Phys. Rev. B 65 (2002) 104426.
[18] J. Lindén, T. Shimada, T. Motohashi, H. Yamauchi, M. Karppinen, Solid State Commun. 129 (2004) 129.
[19] D. Rubi, C. Frontera, J. Nogués, J. Fontcuberta, J. Phys.: Condens. Matter 16 (2004) 3173.
[20] P.-E. Werner, L. Eriksson, M. Westdahl, J. Appl. Crystallogr. 18 (1985) 367.
[21] J. Laugier, B. Bochu, Chekcell: Graphical Powder Indexing, Cell and Space group Assignment Software, http://www.inpg.fr/LMGP.
[22] J. Rodrigues-Carvajal, Physica B 192 (1993) 55.
[23] C. Howard, B.J. Kennedy, P.M. Woodward, Acta Crystallogr. B 59 (2003) 463.
[24] A.M. Glazer, Acta Crystallogr. B28 (1972) 3384.
[25] D.D. Sarma, P. Mahadevan, T. Saha-Dasgupta, S. Ray, A. Kumar, Phys. Rev. Lett. 85 (2000) 2549.
[26] R.I. Dass, J.B. Goodenough, Phys. Rev. B 63 (2001) 064417.
[27] C. Frontera, D. Rubi, J. Navarro, J.L. García-Muñoz, J. Fontcuberta, C. Ritter, Phys. Rev. B 68 (2003) 012412.
[28] R.D. Shannon, Acta Crystallogr. A 32 (1976) 751.
[29] I.D. Brown, J. Chem. Edu. 77 (2000) 1070.
[30] M. Wojcik, E. Jedryka, S. Nadolski, J. Navarro, D. Rubi, J. Fontcuberta, Phys. Rev. B 69 (2004) 100407(R).
[31] W.H. Song, J.M. Dai, S.L. Ye, K.Y. Wang, J.J. Du, Y.P. Sun, J. Appl. Phys. 89 (2001) 7678.
[32] R.M. Thomas, V. Skumryev, J.M.D. Coey, S. Wirth, J. Appl. Phys. 85 (1999) 5384.
[33] A.S. Ogale, S.B. Ogale, R. Ramesh, T. Venkatesan, Appl. Phys. Lett. 75 (1999) 537.